RSC Advances

Single-crystalline Bi2Fe4O9 synthesized by low-temperature co-precipitation: Performance as photo- and Fenton catalysts

Journal:	*RSC Advances*
Manuscript ID:	RA-ART-03-2014-002555.R1
Article Type:	Paper
Date Submitted by the Author:	27-May-2014
Complete List of Authors:	Hu, Zhong-Ting; Nanyang Technological University, Division of Environmental and Water Resources Engineering Chen, Bo; Nanyang Technological University, School of Materials Science and Engineering Lim, Teik-Thye; Nanyang Technological University, Division of Environmental and Water Resources Engineering

Table of contents

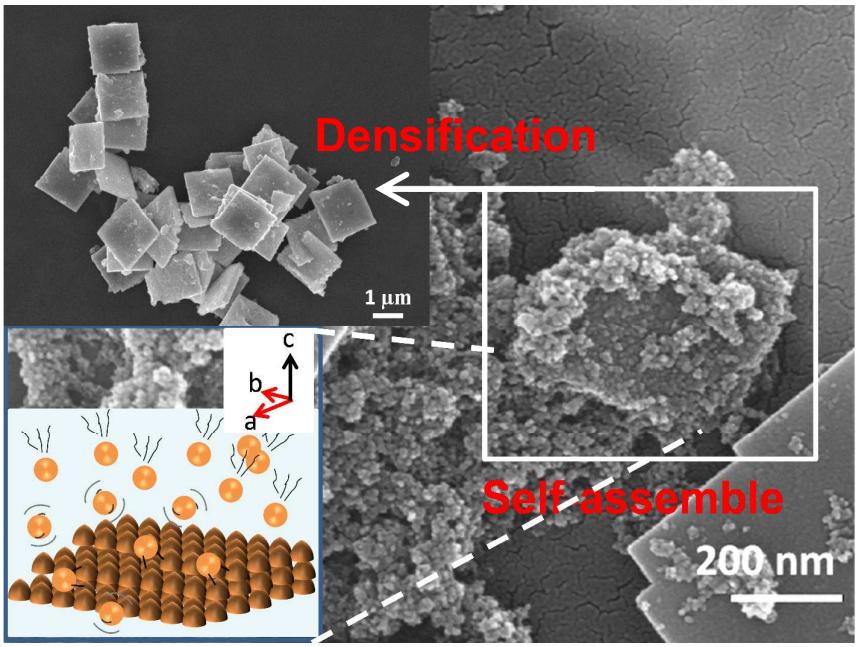

A multi-functional self-assembled (001) $Bi_2Fe_4O_9$ nanopad was firstly synthesized by co-precipitation at 95ºC, which can drive hybrid advanced oxidation processes (HAOPs) under visible-light irradiation for the degradation of bisphenol A efficiently.

RSC Advances

RSCPublishing

PAPER

Single-crystalline $Bi_2Fe_4O_9$ synthesized by low-temperature co-precipitation: Performance as photo- and Fenton catalysts†

Cite this: DOI: 10.1039/x0xx00000x

Received 00th ,
Accepted 00th

DOI: 10.1039/x0xx00000x

www.rsc.org/

Zhong-Ting Hu,[a] Bo Chen,[b] Teik-Thye Lim*[ac]

Multi-functional, self-assembled mullite bismuth ferrites ($Bi_2Fe_4O_9$) have been synthesized by a facile co-precipitation method under a low temperature of 95°C. The Bi/Fe precursor molar ratio and the reaction time were investigated for their influences on the resulting $Bi_2Fe_4O_9$ nanopads. The $Bi_2Fe_4O_9$ nanopads were formed *via* self-assembled crystal growth along the (001) plane, with an average thickness of 170 nm. The most well crystalline nanopads were produced at a reaction time of 36 h, beyond which the nanopads started to dissolve. The produced pure $Bi_2Fe_4O_9$ nanopads exhibit a high degree of elemental stoichiometry with uniform elemental distribution. The $Bi_2Fe_4O_9$ exhibits double bandgaps of 1.9 and 2.3 eV, and shows surface area of 5.8 m^2 g^{-1}. It can be photoexcited by visible light of up to 656 nm. The $Bi_2Fe_4O_9$ can be used as a photocatalyst and Fenton catalyst. Its catalytic activities were evaluated using bisphenol A (BPA) as the model pollutant. Under visible-light irradiation from a solar simulator, 34% of BPA could be removed (compared to only ~3% with Evonik P25) *via* visible-light photocatalysis. With addition of H_2O_2 (16 mM), 54% and 73% of BPA could be removed within 1 h *via* dark Fenton-like and visible-light photo-Fenton reactions, respectively. The $Bi_2Fe_4O_9$ also exhibits a weak magnetism of 0.99 emu g^{-1}. The multi-functional $Bi_2Fe_4O_9$ nanopad has a potential to be used for continuous solar catalytic treatment of wastewater over alternate day/night cycle and is recoverable *via* magnetically-enhanced gravity separation.

1. Introduction

Heterogeneous photocatalysis has the ability to degrade almost all organics with the exception of perfluorinated chemicals.[1] The widely used TiO_2 (P25, Evonik) has a large bandgap which renders it photo-excitable by UV only.[2] Furthermore, the dispersed nanocatalysts are difficult to separate from the treated water. These two disadvantages have hindered a large-scale application of photocatalysis in water and wastewater treatment. To overcome these, a novel catalyst which can be photoexcited by solar light or indoor illumination, and meanwhile can be easily recovered from the treated water is much sought after. In recent years, much attention has been paid on the use of bismuth ferrites in water treatment due to its narrow bandgap of ~2.2 eV and its magnetic property at room temperature.[3, 4] These two properties allow efficient utilization of solar energy and possible catalyst recovery *via* a magnetic separation technique.

Since 1950's, many synthesis methods have been attempted to produce bismuth ferrites. Royen and Swars are the first to successfully synthesize perovskite bismuth ferrites using solid state reactions.[5] Thereafter, different methods such as electrospinning,[6] microwave,[7] sol-gel,[8] hydrothermal,[9] spark plasma sintering,[10] rapid liquid phase sintering[11] and rapid two-stage solid state reaction method[12] were reported. In recent years, the hydrothermal method with or without the assistance of microwave became popular for preparation of bismuth ferrites. Liu et al. investigated the effect of NaOH concentration and reaction time on the synthesis of mullite bismuth ferrites and found that a highly crystalline bismuth ferrites nanoplates with exposing crystal faces (001) could be synthesized in 12 M NaOH at 160ºC for 2 h using a microwave hydrothermal

[a] Division of Environmental and Water Resources Engineering, School of Civil and Environmental Engineering, Nanyang Technological University, 50 Nanyang Avenue, Singapore 639798, Singapore. Email: cttlim@ntu.edu.sg; Tel: +65 6790 6933; Fax: +65 6791 0676
[b] School of Materials Science and Engineering, Nanyang Technological University, 50 Nanyang Avenue, Singapore 639798, Singapore.
[c] Nanyang Environment & Water Research Institute (NEWRI), Nanyang Technological University, 1 Cleantech Loop, CleanTech One, Singapore 637141, Republic Singapore

†Electronic Supplementary Information (ESI) available: Detailed formula derivation for photo-Fenton oxidation. See DOI: 10.1039/b000000x/

method.[13] Moreover, Sun et al. reported that perovskite and sillenite bismuth ferrites could be prepared by a hydrothermal method while adjusting the reaction temperature at 120 and 100ºC, respectively.[14] Furthermore, Zhang et al. discovered that the crystal growth direction of mullite bismuth ferrites could be tuned through adjusting the concentration of NaOH and successfully synthesized mullite bismuth ferrite with varied morphologies using a hydrothermal synthesis at 200ºC. It was proved that nanoplate-like catalysts with exposing facets (001) achieved higher photodegradation performance for methyl orange than that of other morphologies.[15] However, the hydrothermal method still has some challenges for scale-up because of the use of higher pressure and temperature and the detrimental scale-up effect on the resulting product (*e.g.*, easier phase separation, worse element distribution). Herein, we propose a facile co-precipitation method to synthesize bismuth ferrites under a significantly lower temperature (*i.e.* 95ºC) than that of typical hydrothermal methods. To the best of our knowledge, this is the first report on the synthesis of bismuth ferrites using co-precipitation method at such low temperature.

The effects of synthesis parameters for the mullite bismuth ferrites ($Bi_2Fe_4O_9$) and its catalytic performance for organic degradation in aqueous system were evaluated. The crystal growth of $Bi_2Fe_4O_9$ was investigated through adjusting the molar ratio of Bi/Fe and reaction time. A self-assembled growth of $Bi_2Fe_4O_9$ crystallite is proposed as its evolution mechanism. The characteristics of $Bi_2Fe_4O_9$ were investigated systematically using various characterization techniques including XRD, TEM, SEM, EDS, BET, ICP-OES, FT-IR, DRS and VSM. The efficiencies of bisphenol A (BPA) removal through photocatalysis, dark Fenton-like reaction and visible-light photo-assisted Fenton-like oxidation were examined. A proposed reaction mechanism is presented to depict the high-efficient catalytic performance of $Bi_2Fe_4O_9$ in BPA removal. At last, the magnetic property of $Bi_2Fe_4O_9$ was evaluated using VSM.

2. Experimental

2.1. Materials

All the chemicals were of analytical grade and used without further purification. Bismuth (III) nitrate pentahydrate (≥ 98%, VWR), ferric (III) nitrate nonahydrate (≥ 99%, Merck), sodium hydroxide (pellet, Schedelco), nitric acid (1N, Merck), absolute ethanol (99.9%, Fisher chemical), bisphenol A (AR, Merck), hydrogen peroxide (35%, Alfa Aesar), and acetonitrile (HPLC grade, TEDIA) were used in this study. Milli-Q ultrapure water (18.2 MΩ cm) was used for all the experiments.

2.2. Synthesis

$Bi_2Fe_4O_9$ nanopads were prepared *via* the co-precipitation method under low temperature (co-precipitation/low-temperature dehydration route). Typically, a mixture of $Bi(NO_3)_3{\cdot}5H_2O$ and $Fe(NO_3)_3{\cdot}9H_2O$ in individual stoichiometric proportions, such as 0.5:1, 0.48:1 and 0.46:1 by molar ratio, was dissolved in 20 ml of 1 M HNO_3 by ultrasonication for 5 min. Then, 73 ml of 1 M NaOH was instantly added into the solution to adjust the pH to ~8 with rapid stirring. The reaction was carried out at room temperature and ended after 20 min. A brown suspension was obtained and the corresponding cake was collected by centrifugation at 10 000 rpm for 5 min followed by washing with 100 ml of water to remove the residual of nitrate ions (noted as "precursor"). Thereafter, the precursor was dispersed into 80 ml of 12 M NaOH. Then the suspension was transferred into a Teflon vessel and heated at 95°C with constant stirring for 48 h in an oil bath. For further study on the effect of the reaction time, several precursors were prepared at the Bi/Fe molar ratio of 0.48:1 and dispersed into 12 M NaOH following the above mentioned procedure but the reactions were carried out in the oil bath for varied reaction times of 6, 12, 36 and 48 h. The formation of $Bi_2Fe_4O_9$ can be depicted as follows:

$$Bi^{3+} + 2Fe^{3+} + 9OH^- \xrightarrow{RT} Bi(OH)_3 + 2Fe(OH)_3 \quad (1)$$

$$2Bi(OH)_3 + 4Fe(OH)_3 \xrightarrow{\Delta + [OH^-]} Bi_2Fe_4O_9 + 9H_2O \quad (2)$$

After the dehydration process was completed, the reaction was cooled down to room temperature under ambient environment. The precipitate was filtered and then washed with water, followed by rinsing with 10 ml of absolute ethanol twice. At last, the final product was dried using a vacuum freeze dryer at -44ºC overnight.

2.3. Characterization

The crystal growth was investigated using field emission scanning electron microscopy (FESEM, JEOL JSM-7600F) and X-ray diffraction (XRD, Bruker D8 Advance) with Cu-Ka (λ = 1.5418 Å) operated at 40 kV and 40 mA in a 2θ range of 10-70º with a step size of 0.0266º and a scan speed of 1.05 s/step. The purity of products was analyzed by XRD pattern associated with Match software (version 2.1.3). Moreover, the chemical composition and elemental distribution were examined by X-ray Energy Dispersive Spectroscopy (EDS, Oxford Xmax80 LN2 Free). The corresponding cationic stoichiometry was determined by acid digestion followed by analysis of the digestate with inductively coupled plasma-optical emission spectrometer (ICP-OES, Perkin Elmer Optima 2000DV). The $Bi_2Fe_4O_9$ powder were further characterized using transmission electron microscopy (TEM, JEOL JEM-2010), Fourier transform-infrared spectra (FT-IR), UV-vis diffuse reflectance spectra (DRS, Perkin Elmer Lambda 35) and vibrating sample magnetometer (VSM, LakeShore 7400). The specific surface area was calculated using the Brunauer-Emmet-Teller (BET) equation through N_2 adsorption/desorption measurements (Quantachrome Autosorb-1).

2.4. Catalytic evaluation

The resulted $Bi_2Fe_4O_9$ was evaluated for its performance in heterogeneous photocatalysis, Fenton-like reaction and photo-assisted Fenton-like oxidation of bisphenol A (BPA) used as

the model compound. The pH of the reaction system was rather constant at circumneutral value. Typically, the desired amount of the catalyst, which corresponded to 1.5 g L^{-1}, was added into 100 mL of solution containing 15 mg L^{-1} of BPA followed by continuous stirring for 1 h in dark to achieve adsorption/desorption equilibrium. Thereafter, for the heterogeneous photocatalytic reaction, the suspension was illuminated with visible light (420-630 nm) using a solar simulator (Newport, 150 W Xenon arc lamp, one sun) equipped a polycarbonate filter for UV cut-off. A small amount of solution was drawn out from the reaction vessel at each designated time interval, filtered using 0.45 μm cellulose acetate syringe membrane filter, and then determined for BPA concentration. For the Fenton-like reaction, the experiment was carried out in dark with the assistance of 1.63 mmol of H_2O_2 (16.3 mM). For the photo-assisted Fenton-like oxidation, the reaction was carried out with the assistance of visible-light irradiation and 16.3 mM of H_2O_2 concurrently. A high-performance liquid chromatograph equipped with Hypersil GOLD C18 column and Series 200 UV/Vis detector was used to determine the concentration of BPA (HPLC, Perkin Elmer Series200). The conditions were at 220 nm of detector wavelength, a mobile phase of acetonitrile/water (60/40, v/v) and a flow rate of 0.75 mL min^{-1}.

3. Results and discussion

3.1. Effect of the Bi/Fe molar ratio on crystal growth

In the standard crystal unit cell of mullite bismuth ferrites, it is composed of FeO_6 octahedra, FeO_4 tetrahedra and approximate BiO_6 octahedra, simultaneously.[16] Eventually, Bi^{3+} is surrounded by eight O *via* attracting another two O from the other polyhedra centered by Fe^{3+}. This special structure causes the polyhedral shape with a slight distortion, especially for the BiO_6 octahedra. Through this kind of dragging structures, the bismuth ferrite crystallites prefer to grow along the plane of (001), (110) and ($\bar{1}$10), individually. Among them, the crystal growth orientation favors along the (001) plane since it has the lowest surface energy.[13, 15, 17, 18]

Herein, to investigate the influence of the relative amounts of Bi and Fe sources on the crystal growth, the experiment of the varied molar ratio of Bi/Fe was performed. A series of reactions were carried out at maintaining other conditions as 12 M NaOH at 95ºC for 48 h. Fig. 1 shows the XRD patterns of the as-prepared bismuth ferrites with different initial Bi/Fe molar ratios of 0.50, 0.48 and 0.46. According to the standard XRD pattern of mullite bismuth ferrite (JCPDS PDF 04-009-6352), it indicates that the as-prepared samples all are mullite bismuth ferrites (this will be discussed in detail later) and have no obvious evidence of impurities while tuning the Bi/Fe molar ratio from 0.50 to 0.46. In addition, the high intensities of diffraction peaks exhibit that the as-prepared bismuth ferrites have high crystallinity. The main diffraction peaks are attributed to different facets such as (001), (121), (211), (002), (112), (022), (131), (212), (003), (330), (332) and (004). Among them, it is worth noting that the diffraction intensities along the particular facets (ab planes, marked as *) have a significant change while altering the molar ratio of Bi/Fe. As shown in Fig. 1, when the molar ratio of Bi/Fe is 0.50 (scan 2), the maximum diffraction peak is located at 2θ of 28.2º corresponding to the crystal face (121). As Bi/Fe molar ratio decreases to 0.48, the highest diffraction intensity is replaced and the corresponding facet has shifted to (001) (scan 3). It suggests that the dominating orientation of the crystal growth has changed or the crystal is more favorable to grow along the (001) plane, which is beneficial to form a crystal with a large facet (001). With the Bi/Fe molar ratio further reduces to 0.46, the diffraction intensity of facet (001) becomes stronger and the crystal growth along the other ab planes are more active, indicating that the lower Bi/Fe molar ratio not only promotes the crystal growth along the (001) plane, but also causes it to grow along the [001] direction. It will lead to an increase in thickness of crystals. According to a previous report, photocatalytic activities of mullite bismuth ferrites with exposing facet (001) have the order of significance following nanosheet > nanoplate > nanocube.[15] The following discussion will be based on the Bi/Fe molar ratio of 0.48. The product is labeled as $Bi_2Fe_4O_9$.

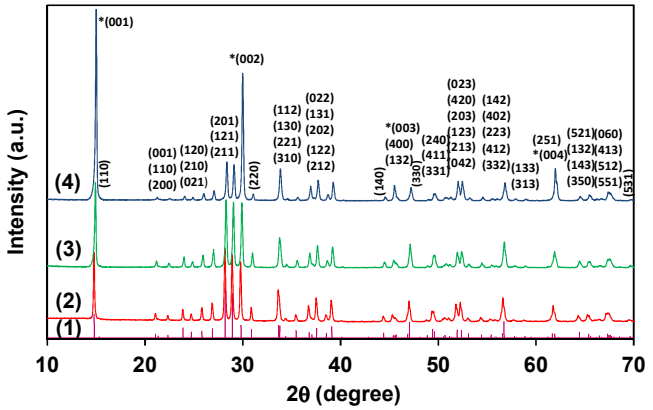

Fig. 1. XRD patterns of standard mullite structure of $Bi_2Fe_4O_9$ (1) and $Bi_2Fe_4O_9$ samples synthesized at various Bi/Fe molar ratio of 0.50 : 1 (2), 0.48 : 1 (3) and 0.46 : 1 (4) (* highlights ab planes).

3.2. Effect of reaction time on crystal growth

Since the crystal growth is a slow process under a normal atmospheric pressure without high energy, the reaction time becomes very important. Through controlling the reaction time, the morphology and size of crystallites can be tuned. Thus, it is worth to study the reaction time to reveal the evolution of the crystal growth of $Bi_2Fe_4O_9$ crystallites. Fig. 2 exhibits SEM images of the $Bi_2Fe_4O_9$ synthesized with varied reaction time of 6, 12, 36 and 48 h. It is obvious that the particle size of $Bi_2Fe_4O_9$ increased from nanometers to micrometers and the morphology changes from sphere-like nanoparticles to square nanopads with an increase in the reaction time. $Bi_2Fe_4O_9$ nanopads show a higher XRD intensity than that of $Bi_2Fe_4O_9$ nanoparticles (Fig. S1). As shown in Fig 2a, uniform

nanoparticles of $Bi_2Fe_4O_9$ formed in 6 h had a typical size of ~6 nm. In Fig. 2b, it is evident that there were various coexisting morphologies of $Bi_2Fe_4O_9$ in 12 h reaction time along with the formed nanopads, and some of them were undergoing formation of nanopads. Fig. 2c shows that regular $Bi_2Fe_4O_9$ nanopads with flat surfaces are formed after 36 h. The size of crystallite has the side length of ~1.5 μm and thickness of ~170 nm. With the reaction time further extended to 48 h, the flat nanopads had turned into broken nanopads with fragmented pieces and uneven surfaces (Fig. 2d).

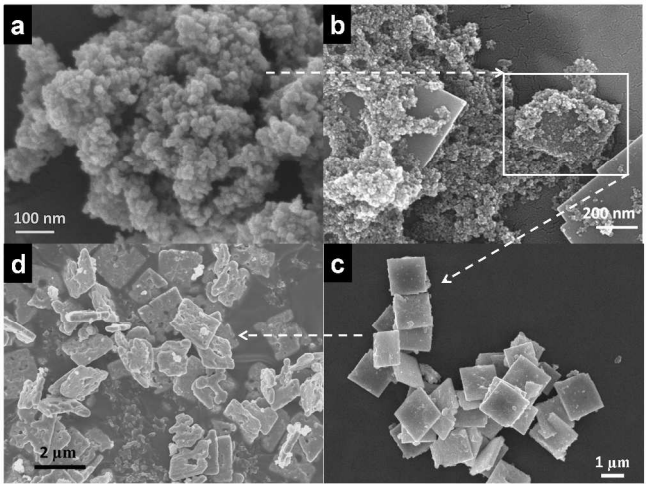

Fig. 2. SEM images of $Bi_2Fe_4O_9$ samples at different reaction times of 6 h (a), 12 h (b), 36 h (c) and 48 h (d).

Based on the above results, a self-assembled evolution of the crystal growth along the plane was proposed. In general, the crystal growth is random along with different orientations and rates due to their different surface energies.[19] However, there is a lower surface energy while $Bi_2Fe_4O_9$ crystallites grow up along the particular crystal faces in the synthesis process, which may contribute to the self-assembled growth of $Bi_2Fe_4O_9$ along a specific plane. Moreover, adjusting the molar ratio of Bi/Fe can help the $Bi_2Fe_4O_9$ crystallites to grow along facet (001). Hence, it is possible to synthesize $Bi_2Fe_4O_9$ nanopads that grow along the (001) plane. As illustrated in Fig. 3, the evolution mechanism of $Bi_2Fe_4O_9$ crystallites includes 4 steps: nucleation and nanoparticle formation, crystal growth with self-assembly, crystal densification and crystal dissolution. In the nucleation and nanoparticle formation stage, the concentration of precursor reaches the critical supersaturation state to nucleate. Nucleation and growth of small crystallites happen simultaneously to result in forming $Bi_2Fe_4O_9$ nanoparticles. With the increase of the reaction time, $Bi_2Fe_4O_9$ nanoparticles tend to aggregrate together along with spontaneous self-organization. This kind of self-organization is going on with the main way of epitaxial extension while subsequently attracting the surrounding $Bi_2Fe_4O_9$ nanoparticles. It will not end until $Bi_2Fe_4O_9$ nanoparticles are exhausted. This kind of crystal growth is similar to self-epitaxy of bismuth ferrites which was reported by Wang et al.[20] In contrast with pulsed laser deposition (PLD), the facile co-precipitation method is low cost, low energy consumption and easy scale-up. Furthermore, the $Bi_2Fe_4O_9$ nanopads composed of nanoparticles will be formed into dense and flat $Bi_2Fe_4O_9$ nanopads. If further prolonged reaction time, the $Bi_2Fe_4O_9$ nanopads will dissolve and recrystallize. The flat surfaces are damaged while generating a lot of pores and forming some fragmented pieces. Thus, the following discussion will be based on the Bi/Fe molar ratio of 0.48 and reaction time of 36 h.

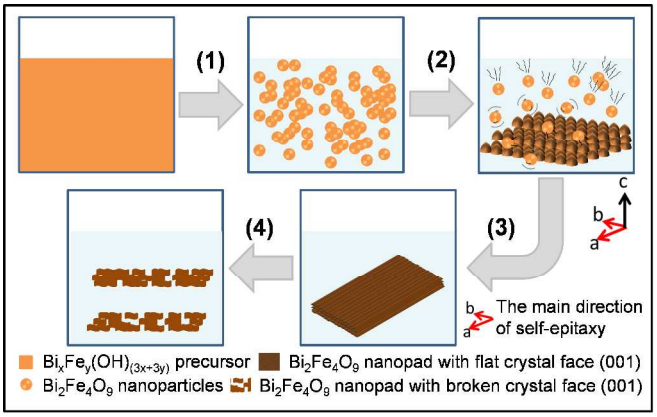

Fig.3. Schematic illustration of the evolution mechanism of $Bi_2Fe_4O_9$ crystallites included nucleation and nanoparticle formation (1), crystal growth with self-assembly (2), crystal densification (3) and crystal dissolution (4).

3.3. Phase purity analysis of $Bi_2Fe_4O_9$ nanopads

Fig. 4 shows XRD patterns of the as-prepared $Bi_2Fe_4O_9$ and different standard samples. Herein, Match software as a fast phase purity analysis is used to characterize the phase compositions of the as-prepared samples. As shown in the figure, it has many crystal plane diffraction peaks marching well with the standard mullite bismuth ferrites ($Bi_2Fe_4O_9$, JCPDS PDF 04-009-6352),[17] indicating the as-prepared $Bi_2Fe_4O_9$ belongs to the space group of orthorhombic crystal system (Pbam) along with many crystal faces and the corresponding diffraction peaks. The main characteristic peaks are located at 2θ of 14.8º, 26.9º, 28.2º, 28.9º, 29.8º, 30.9º, 33.6º, 33.7º, 39.1º, 47.3º and 56.7º.

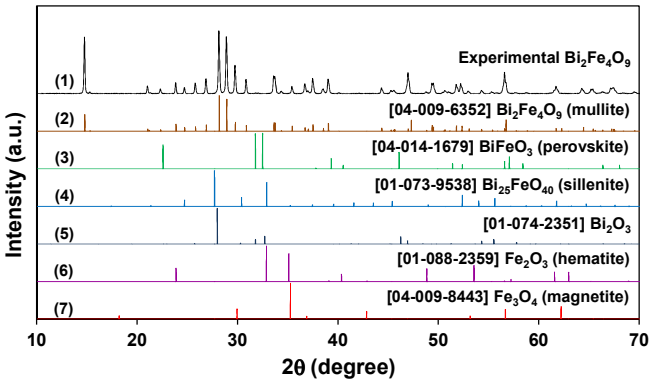

Fig. 4. Phase purity analysis of $Bi_2Fe_4O_9$ sample. The XRD pattern is an experimental sample (1). The standard XRD patterns correspond to mullite $Bi_2Fe_4O_9$ (2), perovskite $BiFeO_3$ (3), sillenite $Bi_{25}FeO_{40}$ (4), Bi_2O_3 (5), hematite Fe_2O_3 (6) and magnetite Fe_3O_4 (7).

Obviously, it is hard to match with the other standard patterns such as perovskite $BiFeO_3$ (04-014-1679),[21] sillenite $Bi_{25}FeO_{40}$ (01-073-9538),[22] Bi_2O_3 (01-074-2351),[23] hematite Fe_2O_3 (01-088-2359)[24] and magnetite Fe_3O_4 (04-009-8443),[25] respectively. For examples, the other phases for bismuth ferrites are the perovskite and sillenite structures. The main diffraction peaks at 2θ for perovskite are 22.6º, 31.8º and 32.5º and for sillenite are 27.7º, 30.4º, 32.9º and 52.4º. Moreover, the possible separated phases of Bi_2O_3, Fe_2O_3 and Fe_3O_4 are also shown in Fig. 4. Bi_2O_3 has main 2θ of 27.9º, 32.7º and 46.3º, Fe_2O_3 has 23.9º, 32.9º and 35.1º, and Fe_3O_4 has 30.0º, 35.3º and 62.2º, respectively. Thus, through the fast phase purity analysis by Match software, it has been shown that the as-prepared sample synthesized using a facile co-precipitation method under low temperature fits well with the standard mullite structure of bismuth ferrites.

3.4. Structure and composition

TEM micrographs of $Bi_2Fe_4O_9$ nanopads at low and high magnifications are shown in Fig. 5a and b. The inset is the corresponding selected area electron diffraction (SAED) pattern along the zone axis [001], confirming the main exposing facets is (001) plane. The TEM image (Fig. 5a) reveals $Bi_2Fe_4O_9$ nanopads have a regular square morphology with the side length of 1.5 μm, which confirms with the result of SEM (Fig. 2c). Moreover, the sharp diffraction spots shown in SAED pattern deduces that the as-prepared $Bi_2Fe_4O_9$ nanopads are single-crystalline,[7, 9] while the $Bi_2Fe_4O_9$ nanoparticles with electron diffraction ring-patterns are poly-crystalline (Fig. S2). Furthermore, the high-resolution TEM (HRTEM) image displays clear lattice fringes with d-spacing of 0.357 nm, which corresponds to the mullite $Bi_2Fe_4O_9$ crystal plane (210) based on JCPDS PDF 04-009-6352.

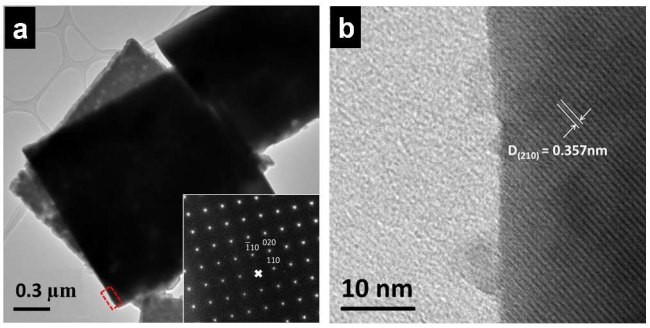

Fig. 5. TEM images of $Bi_2Fe_4O_9$ nanopad and the corresponding SAED pattern (a) and HRTEM image (b).

In addition, in order to monitor the presence of chemical elements and the distribution of them within $Bi_2Fe_4O_9$ nanopads, X-ray Energy Dispersive Spectroscopy (EDS) equipped to the SEM was used to analyze the as-prepared $Bi_2Fe_4O_9$ (Figs. 6 and 7). The chemical elements of Bi, Fe and O are shown in Fig. 6, where the element of C mainly originates from the carbon tape. It reveals that the stoichiometric ratio of Bi/Fe is 0.475, which is similar to the result obtained from digestion of the sample (*i.e.*, 0.476) and is close to the experimental dosage ratio of 0.480. The absolute error (∈) is less than 0.005. Moreover, the elemental distributions of Bi, Fe and O within the $Bi_2Fe_4O_9$ nanopads are very uniform through profiling their elemental distribution mapping (Fig. 7b-d). Thus, it can be concluded that the $Bi_2Fe_4O_9$ nanopad prepared using co-precipitation has the Fe-rich single-crystalline mullite structure along with the uniform elemental distribution.

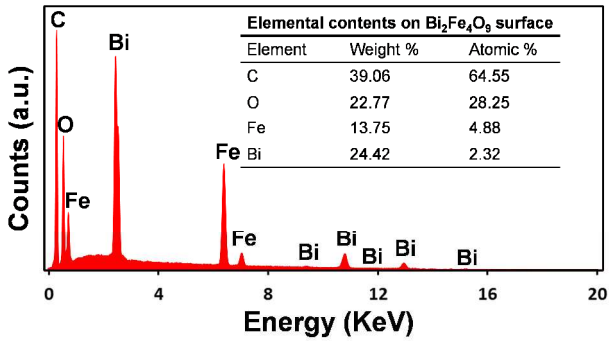

Fig. 6. EDS of $Bi_2Fe_4O_9$ nanopads and the corresponding table of elemental contents (the inset).

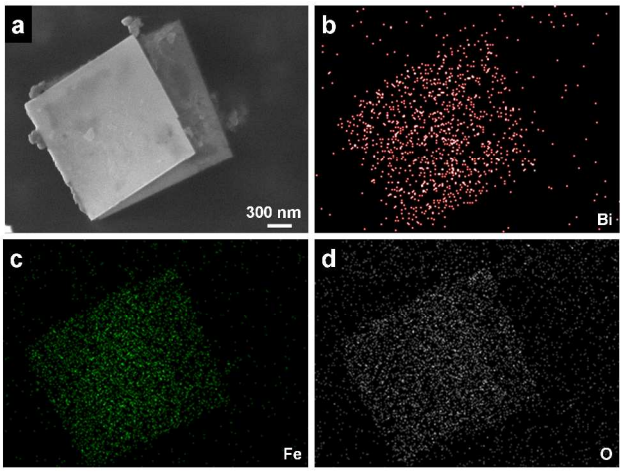

Fig. 7. SEM image of $Bi_2Fe_4O_9$ nanopads (a) and the corresponding elemental distribution mapping of Bi (b), Fe (c) and O (d).

3.5. Surface area and surface property

The photocatalytic activity of a catalyst is directly proportional to its specific surface area because a catalyst with higher surface area possesses more active sites and possibly promotes the separation of electron/hole pairs.[26] Fig. 8a shows the nitrogen sorption isotherm of $Bi_2Fe_4O_9$ nanopads. The specific surface area as calculated using the Brunauer-Emmet-Teller (BET) equation is 5.8 m^2 g^{-1} which is larger than that of the bulk $Bi_2Fe_4O_9$ (0.53 m^2 g^{-1}) synthesized by solid state reaction.[27] It is also larger than the flower-liked $Bi_2Fe_4O_9$ of 4.32 m^2 g^{-1}, which was prepared using a hydrothermal method.[28] It indicates that a co-precipitation method is beneficial to prepare catalyst with a higher surface area.

Additionally, $Bi_2Fe_4O_9$ nanoparticles synthesized at 6 h show a higher specific surface area (Fig. S3).

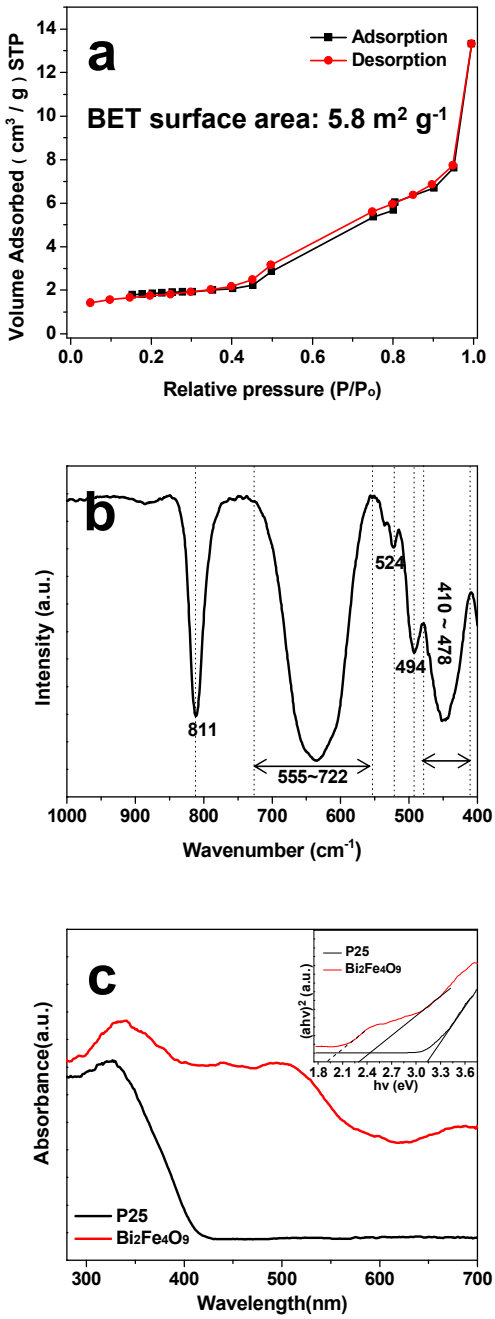

Fig. 8. Nitrogen adsorption/desorption isotherm (a), FT-IR transmittance spectra in the 1000-400 cm^{-1} (b), and UV-vis absorption spectra and the corresponding Kubelka-Munk transformed reflectance spectra (c) of $Bi_2F_4O_9$.

On the other hand, the chemical bonds of $Bi_2Fe_4O_9$ nanopads were characterized for FT-IR spectroscopy. As shown in Fig 8b, the FT-IR transmittance spectrum of $Bi_2Fe_4O_9$ shows three band groups in the 900-800, 800-600 and 600-400 cm^{-1} regions. The single sharp peak at 811 cm^{-1} is assigned to Fe-O stretching vibration of the FeO_4 tetrahedral unit. Moreover, a very broad band from 722-555 cm^{-1} centered at 634 cm^{-1} is attributed to Fe-O stretching vibration of the FeO_4 tetrahedra at 648 cm^{-1}, Fe-O-Fe bending stretching with Fe on both FeO_4 tetrahedral sites at 600 cm^{-1} and Bi-O stretching vibration of the BiO_6 octahedra at 570 cm^{-1}. In general, wavelengths at 524 and 494 cm^{-1} are noted as O-Fe-O bending vibrations of the FeO_4 tetrahedral sites. Furthermore, the other broad absorption band from 478-410 cm^{-1} centered at 448 cm^{-1} is possibly combined by two Fe-O stretching vibrations of the FeO_6 octahedra at 471 cm^{-1} and 437 cm^{-1}, respectively. All of the peak positions shown above are similar to the previous reports,[18, 29, 30] which further confirms that Fe-rich mullite bismuth ferrites have been successfully prepared *via* a facile co-precipitation method under low temperature and indicates the polyhedra present in $Bi_2Fe_4O_9$ crystallites still consist of tetrahedral FeO_4, octahedral FeO_6 and octahedral BiO_6 groups simultaneously.

3.6. Optical property

As shown in Fig. 8c, the UV-vis diffuse reflectance spectra (DRS) of $Bi_2Fe_4O_9$ nanopads and TiO_2 (P25, Evonik) exhibit the different absorption spectra in the wavelength range of 300-700 nm. The result shows that TiO_2 only exhibits photoresponse at wavelengths < 400 nm with an optical bandgap of 3.13 eV, whereas the absorbance of visible light in the range of 400-656 nm becomes stronger for $Bi_2Fe_4O_9$ coupling with two edges of the absorption bands at ~544 and ~656 nm. The corresponding optical bandgaps of 2.3 and 1.9 eV are calculated by the Kubelka-Munk function.[31] It reveals that $Bi_2Fe_4O_9$ is a specific semiconductor with double bandgaps which might correspond to the d-d transitions of Fe.[28] This implies that $Bi_2Fe_4O_9$ can be a visible-light induced photocatalyst. Incidentally, all physicochemical properties of bismuth ferrites, including the as-prepared $Bi_2Fe_4O_9$ and the reported previously, are summarized in Table 1.

Table 1. Physicochemical properties of bismuth ferrites for the as-prepared sample and the previous reported

Characteristics	Experiment results	Ref. results	Ref.
[a]Morphology (nm)	Nanopads with the thickness (170)	Nanoparticle (10-150) Nanoplate (100-200) Nanocube (400-800) Nanofiber (220-480)	6, 7, 13, 15, 28, 32, 33
[b]SSA (m^2 g^{-1})	5.8	0.53	27
[c]Eg (eV)	1.9, 2.3	1.68 - 2.2	3, 14, 34
[d]D-spacing (nm)	0.357	0.23 - 0.42	7, 15, 33
[e]Bi/Fe (by mole)	0.476	0.5, 1.0, 25.0	18, 35, 36
[f]Ms (emu g^{-1})	0.99	0.13 - 3.17	6, 14, 37-39

[a] Particle size was measured through FE-SEM.
[b] Specific surface area was determined by the BET equation.
[c] Band gap energy was derived using Kubelka-Munk function.
[d] Crystal lattice spacing was measured by HRTEM.
[e] Molar ratio of Bi/Fe was analyzed by ICP-OES.

[f] Magnetization was measured by VSM.

3.7. Evaluation of potential applications

3.7.1. Visible-light driven photocatalysis

Fig. 9a shows the degradation of BPA through photolysis and photocatalysis under visible-light irradiation. During 4 h of visible-light irradiation at the wavelength region of 420-630 nm, the removal efficiency of BPA can be negligible (≤ 0.4%) in the absence of $Bi_2Fe_4O_9$ because BPA has an excellent photostability. Photocatalytic degradation with P25 shows only 3% of the initial removal rate of BPA after 1 h (5% for 4 h) because of its limited photoresponce at $\lambda \geq 420$ nm. As compared to P25 at the same catalyst loading, $Bi_2Fe_4O_9$ nanopad exhibits a significant enhancement in the photocatalytic degradation (PCD) rate where 34% of the BPA is removed in the same time period (47% for 4 h) while $Bi_2Fe_4O_9$ nanoparticle also shows the visible-photocatalytic activity (Fig. S4). As shown in the figure, the PCD rate of BPA slows down after 1 h. It could be that the intermediates produced and the products would compete with BPA for active sites on the surface of catalysts. Another plausible postulation is that $Bi_2Fe_4O_9$ shows a lower yield of hydroxyl radicals (OH●) under visible-light irradiation, which will be discussed later.

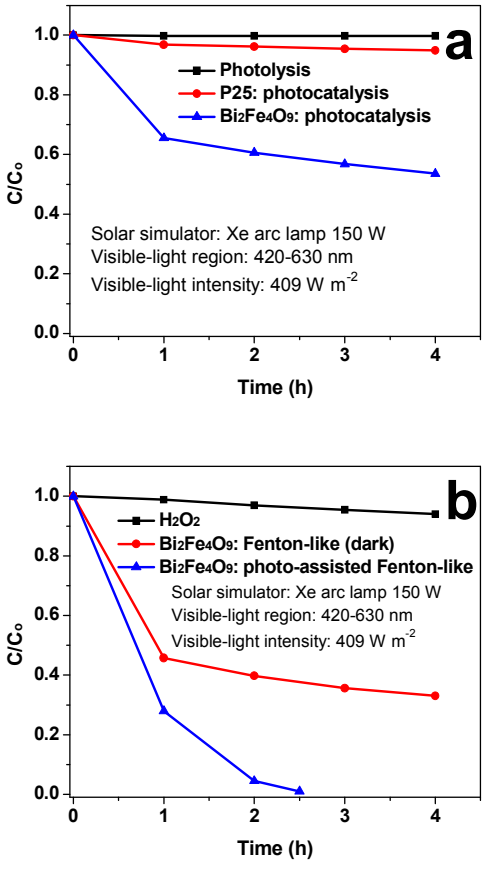

Fig. 9. Performance of $Bi_2Fe_4O_9$ nanopads for degradation of BPA through various processes: (a) photocatalysis, (b) Fenton-like reaction and photo-assisted Fenton-like oxidation.

3.7.2. Fenton-like and photo-assisted Fenton-like reactions

Fig. 9b shows the degradation of BPA through Fenton-like reaction and photo-assisted Fenton-like oxidation. As shown in the figure, the removal efficiency of BPA in the dark by H_2O_2 is only 5% without $Bi_2Fe_4O_9$, whereas it reaches 54% through Fenton-like reaction in the presence of $Bi_2Fe_4O_9$ and H_2O_2 at 1 h (67% for 4 h). Furthermore, it is evident that the removal efficiency of BPA has a significant improvement with the introduction of visible-light irradiation ($420 \leq \lambda \leq 630$ nm) as compared with that of Fenton-like reaction in dark. Through photo-assisted Fenton-like oxidation, 73% of BPA can be removed within 1 h (more than 97% after 2.5 h). Commonly, Fenton-like reactions can be induced under an aqueous system containing iron ions at low pH ~2.8 and it can be negligible for iron ions under circumneutral pH.[40] During the entire reaction process, the pH measured was consistently a range of 6.3-6.5, which suggests the occurance of Fenton-like reaction induced by fictitious $Bi_2Fe_4O_9(Fe^{3+})$ cations. Meanwhile, the fictitious $Bi_2Fe_4O_9(Fe^{3+})$ would be used to discuss the high-efficient photo-assisted Fenton-like oxidation rather than the conventional concept of photodissolution of iron oxides. This is due to the fact that iron oxides are photostable at longer wavelengths (≥ 420 nm) at pH ~7[41] and the iron concentrations as detected in the solution are quite low (*e.g.*, < 0.3 mg L^{-1}) in our reaction solution during the process. In summary, $Bi_2Fe_4O_9$ could exhibit visible-light photocatalysis, Fenton-like reaction and photo-Fenton oxidation, or hybrid advanced oxidation processes (HAOPs). The corresponding reaction mechanisms of HAOPs will be discussed later.

3.7.3. Magnetic property

For the application of heterogeneous catalytic advanced oxidation processes (AOPs) in water treatment, a catalyst owing magnetic properties has attracted considerable interest in recent years.[42] Bismuth ferrites as a kind of multiferroic oxides have more than one property. It has been reported that perovskite bismuth ferrite ($BiFeO_3$) shows a saturation magnetization from 0.13 to 1.55 emu g^{-1},[6, 38] while sellinite bismuth ferrite ($Bi_{25}FeO_{40}$) exhibits a larger saturation magnetization about 2.6-3.17 emu g^{-1}.[14, 39] However, there are few studies on the magnetism of mullite $Bi_2Fe_4O_9$. Herein, we investigated the magnetic property of the as-prepared $Bi_2Fe_4O_9$. The M-H hysteresis loop of the $Bi_2Fe_4O_9$ nanopads was measured at T = 300 K under an appropriate applied field of 14.5 kOe. As shown in Fig. 10, the result exhibits that the saturation magnetization is ~ 0.99 emu g^{-1}, indicating that $Bi_2Fe_4O_9$ nanopads have ferromagnetic properties at room temperature. The magnetic intensity of $Bi_2Fe_4O_9$ is between those of $BiFeO_3$ and $Bi_{25}FeO_{40}$. Although the pristine magnetic intensity of bismuth ferrites is not strong enough, it rightly implies that it has a potential for catalyst recovery from the treated water using magnetic separation technology.

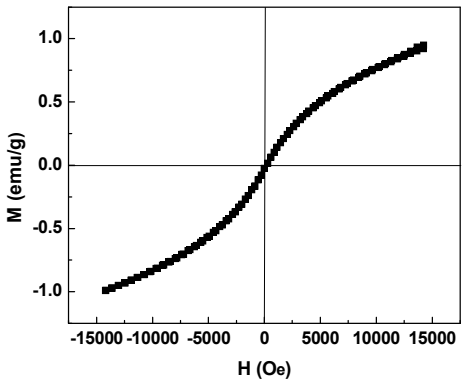

Fig. 10. M-H hysteresis loop of $Bi_2Fe_4O_9$ nanopads measured at T = 300 K.

3.8. Proposed mechanism

Fig. 11 shows the schematic illustration of ROSs generation through $Bi_2Fe_4O_9$-based HAOPs including enhanced photocatalysis by auxiliary H_2O_2, Fenton-like reaction and photo-Fenton oxidation. Typically, during the photocatalytic process using $Bi_2Fe_4O_9$ under visible-light irradiation at pH 6.3-6.5, the mechanism of generation of OH● ($E^o(H_2O_2/OH●)$ = 0.8 V *vs* NHE at pH 7)[43] by conduction band electrons (CBE) can be depicted in Eqs. (3)-(8). The process involves formations of the corresponding reactive oxygen species (ROSs) such as superoxide radicals ($E^o(O_2/O_2●^-)$ = -0.28 V),[44] hydroperoxyl radicals ($HO_2●$, Eq. (5))[45] and autogenerated hydrogen peroxides through termination reactions (Eq. (6))[46] and/or through Eq. (7) ($E^o(O_2●^-/H_2O_2$ = 0.92 V, pH 7).[43] Here a limited amount of OH● was formed under such conditions of both a weak acidic solution and a lower valence band hole about 1.3 V *vs* NHE (conduction band electron is -1.0 V) for $Bi_2Fe_4O_9$,[28] resulting in a lower degradation rate of BPA (Fig. 9a). The reasons are summarized as follow: 1) the amount of autogenerated H_2O_2 is limited by that of $HO_2●$ and $O_2●^-$ formed; 2) it is thermodynamically impossible for the generation of OH● through photogenerated h^+ because of $E^o(OH●/H_2O)$ = 2.27 V at pH 7.[44] Nevertheless, the h^+ might contribute to continuous production of O_2 and stability of pH in the photoreactor (Eq.(9)), where the $E^o(O_2/H_2O)$ = 0.83 V at pH 7.[44] Interestingly, an enhanced photocatalysis might improve BPA degradation with the assistance of auxiliary H_2O_2 (Fig. 11).

$$Bi_2Fe_4O_9 + h\nu \rightarrow h^+ + e^- \quad (3)$$

$$e^- + O_2 \rightarrow O_2●^- \quad (4)$$

$$O_2●^- + H^+ \leftrightarrow HO_2● \qquad pK_1 = 4.8^{45} \quad (5)$$

$$HO_2● + HO_2● \rightarrow H_2O_2 + O_2 \quad (6)$$

$$(\text{or } O_2●^- + e^- + 2H^+ \rightarrow H_2O_2) \quad (7)$$

$$H_2O_2 + e^- + H^+ \rightarrow OH● + H_2O \quad (8)$$

$$4h^+ + 2H_2O \rightarrow 4H^+ + O_2 \quad (9)$$

Another plausible reaction can be the Fenton-like reaction, which can be induced by $Bi_2Fe_4O_9$ in dark at pH 6.3-6.5.[47] Herein, fictitious $Bi_2Fe_4O_9(Fe^{3+})$ cations are introduced to explain reaction mechanisms, which have a similar function as Fe^{3+} (ionic state), and possibly caused by oxygen vacancies and interactions between Fe and Bi atoms. The interconversion between $Bi_2Fe_4O_9(Fe^{3+})$ and $Bi_2Fe_4O_9(Fe^{2+})$ can be described by Eqs. (10)-(11). Similar as a conventional Fenton-like reaction, the fictitious $Bi_2Fe_4O_9(Fe^{3+})$ cations will be transformed to $Bi_2Fe_4O_9(Fe^{3+})(HO_2^-)$ complexes through Eq. (10a) followed by generation of $HO_2●$ *via* Eq. (10b). The corresponding iron-like cycle is shown in the dotted line square (Fig. 11). However, Eq. (10) is a rate-limiting step during the entire Fenton-like process since the reaction rate constant (k) for Eq. (10a) is much lower (k_{10} = 0.001-0.01 M^{-1} s^{-1} for formation of $Fe(HO_2)^{2+}$ at pH 2.8) than that of Eq. (11) (k_{11} = 70 M^{-1} s^{-1}),[48, 49] which leads to retardation of the BPA degradation rate (Fenton-like in Fig. 9b).

$$Bi_2Fe_4O_9(Fe^{3+}) + H_2O_2 \rightarrow Bi_2Fe_4O_9(Fe^{2+}) + H^+ + HO_2● \quad (10)$$

$$Bi_2Fe_4O_9(Fe^{3+}) + H_2O_2 \leftrightarrow Bi_2Fe_4O_9(Fe^{3+})(HO_2^-) + H^+ \quad (10a)$$

$$Bi_2Fe_4O_9(Fe^{3+})(HO_2^-) \rightarrow Bi_2Fe_4O_9(Fe^{2+}) + HO_2● \quad (10b)$$

$$Bi_2Fe_4O_9(Fe^{2+}) + H_2O_2 \rightarrow Bi_2Fe_4O_9(Fe^{3+}) + OH^- + OH● \quad (11)$$

Furthermore, it has been proved that photo-Fenton oxidation can enhance the regeneration rate of Fe^{2+} at pH 2.8 efficiently and can be induced by irradiation with wavelength up to 650 nm (λ_{max}) in the presence of H_2O_2.[50-52] Here an overall equation of the $Bi_2Fe_4O_9$-based photo-Fenton reaction can be described as Eq. (12) (details are shown in ESI). The generated $Bi_2Fe_4O_9(Fe^{2+})$ can also drive Fenton reaction (Eq. (11)). Thus, an iron-like cycle will be activated between Eqs. (11) and (12), which is shown in the bottom right-hand corner of Fig. 11. It also contributes to control the concentration of dissolved O_2 and pH value in the entire system.

$$Bi_2Fe_4O_9(Fe^{3+}) + 2H_2O_2 + h\nu \rightarrow Bi_2Fe_4O_9(Fe^{2+}) + OH● + H_2O + O_2 + H^+ \quad (12)$$

Hence, with the presence of both visible light (420-630 nm) and H_2O_2, the resulting HAOPs can exhibit an enhanced efficiency of $Bi_2Fe_4O_9$ in BPA degradation (photo-assisted Fenton-like in Fig. 9b) that is ascribed to the interaction among enhanced photocatalysis, photo-Fenton oxidation and Fenton-like reaction. In this HAOPs system, H_2O_2 can be autogenerated *via* photocatalysis and initiated Fenton-like reaction, while the solar-driven self-renewal of O_2 also can be used to promote HAOPs (Fig. 11). In the absence of visible light, the auxiliary H_2O_2 needs to be introduced to ensure continuity of AOP in this system, albeit at a slow reaction rate. Nevertheless, it is expected to realize a continuous treatment of wastewater at all hours of the day and night through alternation of AOPs.

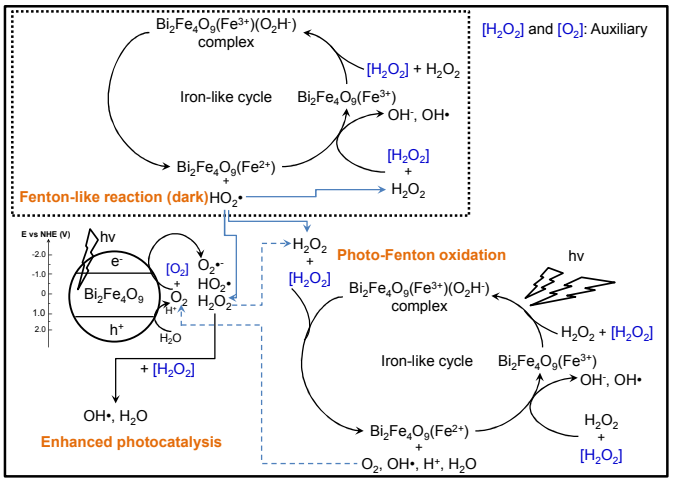

Fig. 11. Schematic illustration of ROSs generation through $Bi_2Fe_4O_9$-based HAOPs (Note: reactions of BPA with ROSs are not shown and simulated visible light at a range of 420-630 nm with UV/IR cut-off).

4. Conclusions

We have successfully developed a facile low-temperature co-precipitation method to prepare self-assembled $Bi_2Fe_4O_9$ nanopads with exposing facet (001). Through investigation of synthesis parameters, it was found out that the molar ratio of Bi/Fe and the reaction time have significant effects on the crystal growth. A corresponding evolution mechanism is proposed. The resulting $Bi_2Fe_4O_9$ have single-crystalline structure with double bandgaps, and possess a high degree of phase purity, crystallinity, element stoichiometry and uniform elemental distributions, and exhibit a relatively higher surface area. It shows its multifunctionality in respect of visible-light photocatalysis, dark Fenton-like reaction and photo-Fenton oxidation. In the presence of both visible light and H_2O_2, a plausible mechanism of hybrid advanced oxidation processes (HAOPs) is illustrated to explain the high efficiency of $Bi_2Fe_4O_9$ in BPA degradation. $Bi_2Fe_4O_9$ also exhibits a weak magnetism at room temperature. This study has a great significance in the synthesis of highly efficient $Bi_2Fe_4O_9$ by an easier scale-up method with low cost and energy saving. It is expected to realize a continuous treatment of wastewater at all hours of the day and night through alternation of solar-driven HAOPs and dark Fenton-like reaction, and catalyst recovery from the treated water by magnetically-enhanced gravity separation.

Acknowledgements

The authors want to thank Nanyang Technological University (NTU) for the award of a PhD research scholarship and all the laboratory staffs for their kind assistance who come from Environmental Lab 1 and Central Environmental Science and Engineering Laboratory (CESEL).

References

1. J. M. Herrmann, *Top Catal*, 2005, **34**, 49-65.
2. Y. Xu and M. A. A. Schoonen, *American Mineralogist*, 2000, **85**, 543-556.
3. F. Gao, X. Y. Chen, K. B. Yin, S. Dong, Z. F. Ren, F. Yuan, T. Yu, Z. G. Zou and J. M. Liu, *Advanced Materials*, 2007, **19**, 2889-2892.
4. G. Catalan and J. F. Scott, *Advanced Materials*, 2009, **21**, 2463-2485.
5. P. Royen and K. Swars, *Angew. Chem.*, 1957, **69**, 779.
6. W. Wang, N. Li, Y. Chi, Y. Li, W. Yan, X. Li and C. Shao, *Ceramics International*, 2013, **39**, 3511-3518.
7. U. A. Joshi, J. S. Jang, P. H. Borse and J. S. Lee, *Applied Physics Letters*, 2008, **92**, 242106.
8. F. Yan, G. Zhao and N. Song, *Journal of Rare Earths*, 2013, **31**, 60-64.
9. L. Wu, C. Dong, H. Chen, J. Yao, C. Jiang and D. Xue, *Journal of the American Ceramic Society*, 2012, **95**, 3922-3927.
10. Z.H. Dai and Y. Akishige, *Journal of Physics D: Applied Physics*, 2010, **43**, 445403.
11. Y. P. Wang, L. Zhou, T. C. M. F. Zhang, T. C. X. Y. Chen, T. C. J. -M. Liu and Z. G. Liu, *Applied Physics Letters*, 2004, **84**, 1731-1733.
12. V. A. Khomchenko, D. A. Kiselev, J. M. Vieira, L. Jian, A. L. Kholkin, A. M. L. Lopes, Y. G. Pogorelov, J. P. Araujo and M. Maglione, *Journal of Applied Physics*, 2008, **103**, 024105.
13. Z. Liu, B. Wu and Y. Zhu, *Materials Chemistry and Physics*, 2012, **135**, 474-478.
14. Y. Sun, X. Xiong, Z. Xia, H. Liu, Y. Zhou, M. Luo and C. Wang, *Ceramics International*, 2013, **39**, 4651-4656.
15. X. Zhang, J. Lv, L. Bourgeois, J. Cui, Y. Wu, H. Wang and P. A. Webley, *New Journal of Chemistry*, 2011, **35**, 937-941.
16. A. Friedrich, E. A. Juarez-Arellano, E. Haussühl, R. Boehler, B. Winkler, L. Wiehl, W. Morgenroth, M. Burianek and M. Mühlberg, *Acta Crystallographica Section B: Structural Science*, 2010, **66**, 323-337.
17. E. Kostiner and G. L. Shoemaker, *Journal of Solid State Chemistry*, 1971, **3**, 186-189.
18. M. M. Murshed, G. Nénert, M. Burianek, L. Robben, M. Mühlberg, H. Schneider, R. X. Fischer and T. M. Gesing, *Journal of Solid State Chemistry*, 2013, **197**, 370-378.
19. X.-Z. Chen, Z.-C. Qiu, J.-P. Zhou, G. Zhu, X.-B. Bian and P. Liu, *Materials Chemistry and Physics*, 2011, **126**, 560-567.
20. J. Wang, J. B. Neaton, H. Zheng, V. Nagarajan, S. B. Ogale, B. Liu, D. Viehland, V. Vaithyanathan, D. G. Schlom, U. V. Waghmare, N. A. Spaldin, K. M. Rabe, M. Wuttig and R. Ramesh, *Science*, 2003, **299**, 1719-1722.
21. P. Ravindran, R. Vidya, A. Kjekshus, H. Fjellvåg and O. Eriksson, *Physical Review B*, 2006, **74**, 224412.
22. C. E. Infante and B. Carrasco, *Materials Letters*, 1986, **4**, 194-197.
23. G. Gattow and D. Schutze, *Zeitschrift fur Anorganische und Allgemeine Chemie*, 1964, **328**, 44-68.
24. M. Catti, G. Valerio and R. Dovesi, *Physical Review B*, 1995, **51**, 7441-7450.
25. H. Okudera, K. Kihara and T. Matsumoto, *Acta Crystallographica Section B: Structural Science*, 1996, **52**, 450-457.
26. A. T. Bell, *Science*, 2003, **299**, 1688-1691.

27. T.-J. Park, G. C. Papaefthymiou, A. R. Moodenbaugh, Y. Mao and S. S. Wong, *Journal of Materials Chemistry*, 2005, **15**, 2099-2105.
28. S. Sun, W. Wang, L. Zhang and M. Shang, *The Journal of Physical Chemistry C*, 2009, **113**, 12826-12831.
29. M. I. Aroyo, J. M. Perez-Mato, C. Capillas, E. Kroumova, S. Ivantchev, G. Madariaga, A. Kirov and H. Wondratschek, *Zeitschrift fur Kristallographie*, 2006, **221**, 15-27.
30. D. Voll, A. Beran and H. Schneider, *Phys Chem Minerals*, 2006, **33**, 623-628.
31. SHIMADZU, *Application News: spectrophotometric analysis*, A428.
32. Z. Liu, Y. Qi and C. Lu, *Journal of Materials Science: Materials in Electronics*, 2010, **21**, 380-384.
33. K. L. Da Silva, D. Menzel, A. Feldhoff, C. Kübel, M. Bruns, A. Paesano, A. Düvel, M. Wilkening, M. Ghafari, H. Hahn, F. J. Litterst, P. Heitjans, K. D. Becker and V. Šepelák, *Journal of Physical Chemistry C*, 2011, **115**, 7209-7217.
34. P. Fischer, M. Polomska, I. Sosnowska and M. Szymanski, *Journal of Physics C*, 1980, **13**, 1931.
35. S. M. Selbach, M. A. Einarsrud and T. Grande, *Chemistry of Materials*, 2009, **21**, 169-173.
36. A. Sun, H. Chen, C. Song, F. Jiang, X. Wang and Y. Fu, *RSC Advances*, 2013, **3**, 4332-4340.
37. V. Kothai and R. Ranjan, *Bulletin of Materials Science*, 2012, **35**, 157-161.
38. T.-J. Park, G. C. Papaefthymiou, A. J. Viescas, A. R. Moodenbaugh and S. S. Wong, *Nano Letters*, 2007, **7**, 766-772.
39. G.-Q. Tan, Y.-Q. Zheng, H.-Y. Miao, A. Xia and H.-J. Ren, *Journal of the American Ceramic Society*, 2012, **95**, 280-289.
40. A. Babuponnusami and K. Muthukumar, *Journal of Environmental Chemical Engineering*, 2013.
41. M. I. Litter and M. A. Blesa, *Journal of Colloid and Interface Science*, 1988, **125**, 679-687.
42. C. Marichy, M. Bechelany and N. Pinna, *Advanced Materials*, 2012, **24**, 1017-1032.
43. P. Wardman, *Journal of Physical and Chemical Reference Data*, 1989, **18**, 1637-1755.
44. A. Fujishima and X. Zhang, *Comptes Rendus Chimie*, 2006, **9**, 750-760.
45. B. H. J. Bielski, D. E. Cabelli, R. L. Arudi and A. B. Ross, *Journal of Physical and Chemical Reference Data*, 1985, **14**, 1041-1100.
46. A. J. Hoffman, E. R. Carraway and M. R. Hoffmann, *Environmental Science & Technology*, 1994, **28**, 776-785.
47. F. Velichkova, C. Julcour-Lebigue, B. Koumanova and H. Delmas, *Journal of Environmental Chemical Engineering*, 2013, **1**, 1214-1222.
48. C. Walling and A. Goosen, *Journal of the American Chemical Society*, 1973, **95**, 2987-2991.
49. T. Rigg, W. Taylor and J. Weiss, *The Journal of Chemical Physics*, 1954, **22**, 575-577.
50. J. J. Pignatello, *Environmental Science & Technology*, 1992, **26**, 944-951.
51. J. J. Pignatello, D. Liu and P. Huston, *Environmental Science & Technology*, 1999, **33**, 1832-1839.
52. W. H. Koppenol, J. Butler and J. W. v. Leeuwen, *Photochemistry and Photobiology*, 1978, **28**, 655-658.

